doi:10.20944/preprints202010.0579.v1

Article

Probing the analytical cancelation factor of short scale gravity waves using Na lidar and nightglow data from the Andes Lidar Observatory

Fabio Vargas[1,‡], Javier Fuentes[2,‡], Pedro Vega[3], Luis Navarro[1], and Gary Swenson[1]

[1] Department of Electrical and Computer Engineering, Remote Sensing & Space Science Laboratory, University of Illinois at Urbana-Champaign, Urbana, Illinois, USA; fvargas@illinois.edu, swenson1@illinois.edu, lnav@illinois.edu

[2] Gemini Observatory Southern Operations Center, Av. Juan Cisternas 1500, c/o AURA casilla 603, La Serena, Chile; jfuentes@gemini.edu

[3] Faculty of Science, Physics Department, University of La Serena, Av. Juan Cisternas 1200, La Serena, Chile; pvega@userena.cl

‡ These authors contributed equally to this work.

Abstract: The cancelation factor (CF) is a model for the ratio between gravity wave perturbations in the airglow intensity to that in the ambient temperature. The CF model allows to estimate the momentum and energy flux of gravity waves seen in nightglow images as well as the divergence of these fluxes due to waves propagating through the mesosphere and lower thermosphere region, where the nightglow and the Na layers are located. This study uses a set of T/W Na Lidar data and zenith nightglow image observations of the OH and $O(^1S)$ emissions to test and validate the CF model from the experimental perspective. The dataset analyzed was obtained during campaigns carried out at the Andes Lidar Observatory (ALO), Chile in 2015, 2016, and 2017. The CF modeled function was compared with observed points from an empirical method for vertically propagating waves that calculates directly the ratio of the gravity wave amplitude seen in nightglow images to the wave amplitude seen in lidar temperatures. We show that the CF analytical relationship underestimates the observed results generally. However, the O(^{1}S) emission line has better agreement respect to the theoretical value due to simpler nightglow photochemistry. In contrast, the observed CF ratio from the OH emission deviates by a factor of two from the modeled asymptotic value.

Keywords: Airglow; All-Sky Imagery; Atmospheric Gravity Waves; Cancelation Factor; Lidar; Mesosphere-Lower-Thermosphere.)

---

1. Introduction

Propagating Atmospheric Gravity Waves (AGWs) perturb the density and composition of major and minor species in the Mesosphere and Lower Thermosphere (MLT). These species are part of a chain of complex chemical reactions as a result of solar ultraviolet radiation which ultimately leads to airglow emissions [e.g., 1–4]. Airglow emission brightness fluctuations have been the focus of different studies using one-dimensional models upon certain atmosphere conditions for gravity waves with various intrinsic parameters and damping rates ([e,g., 5–8]).

The ratio of the relative perturbation in intensity $\frac{I'}{\bar{I}}$ to that in ambient temperature $\frac{T'}{\bar{T}}$, known as the *cancelation factor* (CF=$\frac{I'/\bar{I}}{T'/\bar{T}}$), is used to determine how the layer responds to wave perturbations of various vertical scales. An analytical expression for the cancelation factor (CF) was first derived by [5] for the OH nightglow brightness, which is defined as the height integral over layer's volume emission rate (VER), relating this brightness to the temperature perturbation at the altitude of maximum VER. The CF expression from [5] was used in [6] to relate measurements of gravity wave energy and momentum flux in several instruments. [7] extended the modeling study for the $O_2(b, 0-1)$ atmospheric bands and OH Meinel emission allowing to investigate the relations between the amplitude and phase of the airglow perturbations induced by gravity waves from simultaneous measurements in both layers. Finally, [8] presented a comprehensible one-dimensional model adding the $O(^1S)$ emission line to the study of the night airglow emission in response to the AGW perturbations to explore the vertical flux of horizontal momentum and their wave effects on the atmosphere from the three $O(^1S)$, OH, and $O_2(b)$ airglow layers. The latter study drove the motivation to derive the uncertainties in momentum flux and accelerations due to gravity wave parameters estimated from mesospheric nightglow emissions reported in [9].

We present the first study of the empirical assessment of the cancelation factor using Na lidar data and nightglow all-sky imagery of the OH and $O(^1S)$ emissions during the observing campaigns during the 2015, 2016, and 2017 at the Andes Lidar Observatory (ALO) over Chile. We provide the magnitude of CF for multiple waves detected during these campaigns and directly compare these observation with the modeled CF.

2. Instrumentation and Methodology

The Andes Lidar Observatory (ALO) is an facility for middle and upper atmosphere studies located at 30.3°S, 70.7°W at an altitude of 2530 m near to Cerro Pachón, Chile. The ALO facility was designed to investigate wave dynamics including the influence of mountain waves in the mesosphere and lower thermosphere (MLT) region. It is equipped with a suite of passive optical instruments including a Na resonance-fluorescence lidar, and all-sky airglow imagers. ALO also houses a meteor radar, and a Mesospheric Temperature Mapper (MTM) camera.

The lidar system has nominal power of 1.5 mW to obtain temperature, wind velocity, and Na density profiles typically at resolution of 1 minute, 500 meters between 80–105 km. Observations using the Na lidar and nightglow imagery system are carried out in low Moon periods throughout the year. All-sky images of the nightglow are taken simultaneously with the lidar, and individual gravity wave occurrence in both systems can be monitored during the observation time.

The ALO all-sky imagers record nightglows of hydroxyl $OH(6,2)$ Meinel bands and atomic oxygen line emissions as seen in Fig. 1. At preprocess, each individual image is mapped onto an uniform, 512×512 km^2 grid of pixels in geographical coordinates with a resolution of 1 km/pixel. The assumed altitudes for the OH and $O(^1S)$ emissions are 88 km and 95 km, respectively. The integration time for the OH is 60 s and 90 s for the $O(^1S)$. The imager ASI-1 collects the night airglow emissions using the instrumental configuration presented in Table 1.

The Na lidar is operated in zenith and off-zenith modes to measure the wind and temperature using the three-frequency technique (see, [10]). The laser is locked at the Na resonance frequency at the D2a line, and the two frequencies shifted by ±630 MHz in a sequence. The temperature and line-of-sight wind are derived based on the ratios among the back-scattered signals at these three frequencies as described in [11]. Profiles of Na lidar wind and temperature are shown in Fig. 2. The integration time in each direction varies between campaigns from 60 to 90 sec, that depends on the signal-to-noise ratio retrieved from the photon return.

Table 2 and table 3 summarize the imaging and lidar data set obtained at the Andes Lidar Observatory (ALO) at the campaigns carried out during 2015, 2016, and 2017. We have detected prominent AGWs from the image processing in 85 and 60 out of 100 nights of the initial sample for the $OH(6,2)$ Meinel band emission and $O(^1S)$ emission line, respectively.

The night airglow emission in response to AGWs perturbations was modeled in [8] using a linear, one-dimensional model to describe the temporal and spatial variability of the airglow VER and derive the 1-dimensional cancelation factor parameter. The photochemistry involved in the leading processes to $O(^1S)$ production and the OH Meinel band spectrum as well as the intensity and weighted temperature due to upward propagating Atmospheric Gravity Waves is described in [8].

There were considered a number of assumptions in the [8] model including, for instance, the wave amplitudes are small, so that the linear equations can be used to describe AGWs through their polarization and dispersion relationships. Also, a wave perturbation of 1% amplitude in temperature

doi:10.20944/preprints202010.0579.v1

at a reference altitude of $z_r = 85$ km, the background atmosphere specified by the MSIS00 model is unchanged by the waves (e.g., [12]), a windless atmosphere (no shear with altitude), and the waves are propagating vertically through the layers. The simulations consisted in varying the vertical wavelength, λ_z, and the damping coefficient, β, for a single AGW in order to investigate the relationship between wave perturbations, the vertical wavelength, and the VER of the emissions.

The methodology to obtain analyzes the perturbations in the airglow intensity in response to gravity waves through the wave cancelation effects via CF model. We use the CF empirical model defined as the ratio of the amplitude of I' or T' to the amplitude of the perturbing AGWs at 88 km for OH Meinel band emission and 95 km for $O(^1S)$ emission line. The observed CF is defined for the airglow intensity as $CF = A_I/A_T$. Here, $A_I = I'/\bar{I}$ and $A_T = T'/\overline{T}$, where primed quantities refer to the wave fluctuation and bar quantities to the unperturbed background. A_I is obtained from OH and $O(^1S)$ airglow images processing, and A_T from the lidar temperature data at the time of wave perturbation occurrence in the airglow.

Intrinsic wave parameters from the image dataset (such as the horizontal wavelength (λ_h), wave orientation (θ), wave phase (ϕ), wave period (τ), horizontal phase velocity (c), and the relative wave amplitude ($A_I = I'/\bar{I}$)) have been obtained by performing usual preprocessing routines (i.e., dewarping, star removal, coordinate transformation, detrending, and filtering as described in [13]). In particular, we use mean horizontal winds from the lidar to perform Doppler correction of wave periods. In order to compute the temperature perturbations $A_T = T'/\overline{T}$ from lidar, we have removed the mean ($\overline{T}$) of each temperature altitude to determine $T' = T - \overline{T}$ corresponding to the nominal altitude of the observed nightglows. Then, after selecting short wave periods ($\tau < 1$ hour) from prominent gravity wave events detected in imaging data, we estimate the observed cancelation factor for the two nightglow emissions for these prominent waves.

AlsoThe range of the relative amplitudes in temperature A_T and airglow intensity A_I have been chosen to not break the linearity of the solutions. This way, the dispersion and polarization equations remain valid throughout the analysis. The uncertainty in λ_z was derived using equations (8) and (12) reported in [9]. We verify in this way that σ_{λ_z} increases while λ_z decreases.

Table 4 presents the criteria to filter out undesirable wave parameters obtained from the image processing to us to obtain valid data points for comparison between observed versus modeled CF. Here, z_r is the altitude to obtain the wave amplitude in T for each nightglow layer, which is done by extracting the relative intensity ($I'/\bar{I}$) of the wave. Again, I' and $\bar{I}$ are the perturbed and non-perturbed airglow intensity from the images, while $T'/\overline{T}$ represents the relative wave amplitude in the lidar temperature, T' is the perturbed temperature and $\overline{T}$ represents the non-perturbed temperature obtained at the nominal altitudes of the observed nightglows. Thus, the ratio between I and T perturbations is our experimental estimation of the magnitude of CF.

After filtering the prominent wave events presented in table 2 using the above criteria, we have got for the OH band emission 94 waves events remained on 11 nights in 2015, 113 waves through 19 nights in 2016, and 30 waves on 4 nights in 2017's campaign. Following the same filtering procedure for the $O(^1S)$ emission line, we found 43 wave events remained along 9 nights in 2015, 50 waves appeared during 9 nights in 2016, and 98 AGWs throughout 5 nights in 2017 respectively.

Finally, we have taken the relative wave and temperature intensities to compare the observed cancelation factor against the modeled CF relationship in [8]. The uncertainties showed in this paper have been derived by using equation (11) and their fitting coefficients presented in Table 1, and equation (12), of [9].

3. Results

The observed CF is estimated for both $OH(6,2)$ and $O(^1S)$ emission during 2015, 2016, and 2017 as shown in Figure 3. The measurement of CF values for the OH emission deviate from the theoretical CF relationship (black continuous line in the graphs) more than $O(^1S)$, showing in the latter emission a better agreement in the range of $\lambda_z \sim 20 - 60$ km.

Preprints (www.preprints.org) | NOT PEER-REVIEWED | Posted: 28 October 2020 doi:10.20944/preprints202010.0579.v1

The uncertainties have been derived for λ_z at the OH and $O(^1S)$ emission altitudes. The average value is $\sigma_{\lambda_z} \sim 16\%$ and $\sigma_{\lambda_z} \sim 17\%$ for the OH and $O(^1S)$ emission, respectively. Reference [9] found that λ_z shows uncertainties of ~10% and 8% for OH and $O(^1S)$ emissions. The estimated uncertainties in observed CF is $\sigma_{CF} \sim 10\%$ for OH emission and $\sigma_{CF} \sim 7\%$ for the green line $O(^1S)$, respectively. The dashed thin lines in Figure 3 are the 95% confidence levels derived for the modeled CF curve in the model. The uncertainties for both emissions range between 15-24%, and are higher for shorter λ_z. Some observed CF data points fall within the modeled CF confidence levels (black dashed line) for the OH emission (comparable to the full sample), which indicates those points are in agreement with the modeled CF relationship.

To estimate how far the data points fall from the modeled CF curve, we have built histograms and kernel density estimators (KDE) for the samples. Figure 4 shows the residuals between the observed and modeled CF data points. The sample have been filtered out using a 3σ standard deviation to remove the outliers.

The KDE curve (solid red line) shows the density plot as a smoother version of the histogram. The histogram is normalized by default so that it has the same y-scale as the density plot. Also, we have fitted a Gaussian function with bin width following Freedman-Diaconis rule, which changes the distribution drawn at each data point and the overall distribution. However, we have decided to use the Gaussian kernel density estimation to compute the mean values for both normal distributions.

The histograms in Figure 4 have a well defined central tendency in the normal distribution for both OH and $O(^1S)$ emissions. The center of the $\text{CF}_{O(^1S)}$ is closer to zero than CF_{OH} according to the mean value of the Gaussian curves. The peak of the distribution for both emissions is found to be skewed to the right, meaning that the model underestimates the observed values. The arithmetic mean values have been derived for the OH and $O(^1S)$ emissions as $\mu_{OH} = 3.1$ and $\mu_{O(^1S)} = 1.42$, respectively.

The main contribution of this work is to test the modeled CF relationship using the observed data, and we have verified that the theoretical model underestimate the observations. It is important to measure this discrepancy to make corrections to the theoretical relationship for both emissions. To do so, we have evaluated the discrepancy between observed and modeled CFs, and add them to the corresponding modeled CF for each layer to obtain corrected predictions. To estimate the discrepancy, we define the weighted mean and the standard deviation of the mean of the corrected cancelation factor as

$$\overline{CF} = \frac{\sum_{i=1}^{n} \frac{CF_i}{\sigma^2_{CF_i}}}{\sum_{i=1}^{n} \frac{1}{\sigma^2_{CF_i}}} \tag{1}$$

and

$$\sigma_{\overline{CF}} = \frac{1}{\sqrt{\sum_{i=1}^{n} \frac{1}{\sigma^2_{CF_i}}}}. \tag{2}$$

We computed the weighted mean and standard deviation as they serve as a measure of the spread in the data. Thus, data points presenting smaller uncertainties (σ_{CF}), that is, higher accuracy of the measurements, will have more significant influence on the mean. This is better than using the arithmetic mean and standard deviation that just ignore the magnitude of the error in each measurement. The results are listed in Table 5.

The CF weighted mean and weighted errors computed for $O(^1S)$ emission line in 2015, 2016, and 2017 are in good agreement to the modeled asymptotic value, $\text{CF}_{O(^1S)}$ = 5.1 for large values of λ_z. On the other hand, we did not find a good result for CF_{OH} = 3.8 asymptotic value as the estimated weighted mean is higher than the model in the large wavelength range. However, our findings help to correct the modeled CF relationship for the OH emission. Uncertainties derived for CF data points have

doi:10.20944/preprints202010.0579.v1

been computed for both emissions. Using the weighted mean values as measure of the discrepancies between modeled and observed CFs for a given layer, the modeled curve is then corrected according to the observation. Figure 5 shows the corrected modeled CF for both emissions after the weighted mean was added to their corresponding values.

4. Discussion

We have tested the modeled cancelation factor presented in [8] for the Meinel OH band emission and $O(^1S)$ emission line using observed data obtained from the Andes Lidar Observatory (ALO). We have reported perturbations in the airglow intensity in response to the AGWs under cancelation effect modeled with an empirical method that considers a windless and isothermal atmosphere with upward propagating and saturated waves (the wave amplitude does not change with altitude). Figure 3 shows the cancelation factor in both layers as functions of λ_z. From the definition we see that smaller CF corresponds to a stronger cancelation effect. On the other hand, CF increases with increasing λ_z up to an asymptotic value above the unit, showing that the wave amplitude is being amplified by the layer response to the wave perturbation.

The intensity perturbations with small vertical scale ($\lambda_z < 10$ km) have strong cancelation in the layer because of the finite thickness of the airglow layers, which implies that these short λ_z waves do not show significant amplitudes from ground observations ([7]). Thus, the airglow is not sensitive to these waves. Equation (11) presented in [9] shows that the analytical function describing CF increases monotonically with $\lambda_z > 13$ km for OH band emission and $\lambda_z > 10$ km for $O(^1S)$ emission line, therefore, for λ_z lower than these limits the cancelation effect gets stronger.

The centroid heights and thickness (FWHM) of the unperturbed and standard deviation of the VER profiles derived for the OH layer is larger than that the $O(^1S)$ layer (see Table 1 in Reference [8]), which results in a stronger cancelation effect in the OH layer and therefore the CFs for $O(^1S)$ emission is larger than that for OH, indicating that the greenline airglow is more sensitive to AGWs. For λ_z larger than ~ 20 km, the layer thickness becomes irrelevant because the layer thickness is a fraction of the vertical wavelength; the layer response is stronger and than virtually the same for longer vertical wavelength waves.

The work of [9] has presented a comprehensive discussion about the magnitude of the uncertainties in gravity wave parameters estimated from nightglow measurements, and how these uncertainties affect the estimation of key dynamic quantities in the mesosphere and lower thermosphere region. In this study, we have derived the uncertainties in CF and vertical wavelengths which are subject to large uncertainties. However, these magnitudes are in agreement with conclusions reported in [9].

A source of discrepancy between the modeled and observed CF values found in this study is that the CF model considers saturated waves only. In a real atmosphere, saturated waves co-exist with dissipative and freely propagating waves. That likely accounts for the majority of the discrepancy in our results because we have not separated waves by their kind in this study, that is, all observed wave cases go into our analysis for comparisons with the CF model, and we can not guarantee that the observed waves are saturated waves as considered in the model.

Another source of discrepancy of our results with the modeled CF for the OH and $O(^1S)$ layers is relative to the distribution of atomic oxygen with height in the presence of vertically propagating waves that could also influence the results here. The waves influence the temperature gradient that affect the rate of chemical reactions of the nightglow emissions ([5]). The distribution of species involved in airglow emissions varies considerably with latitude and time, constituting another source of discrepancy between model and measurements ([14]), once the model consider only calm, low solar cycle atmospheric conditions.

Also, based on a full–wave model with the relevant chemistry to the airglow emissions that considers more physical processes such as propagating gravity waves in a non–isothermal mean state, windy (background winds $\neq 0$ as a function of height), and viscous atmosphere, the cancelation factor can vary considerably by a factor of two greater than their isothermal and windless values for gravity waves of short horizontal wavelength with phase velocities less than 100 m/s, and by a factor of one hundred for phase speeds less than 40 m/s as reported in [14].

All in all, having tested the modeled CF relationship against observed data for two airglow layers, we have found that the modeled CF underestimates the observations for both emissions. The cancelation effect is found to be larger in magnitude for OH band emission than for the $O(^1S)$ emission line. However, CF is still a valuable parameter to retrieve the magnitude of the relative temperature fluctuation from the airglow, which is used to estimate the momentum flux magnitude transported by the waves ([9]).

5. Conclusions

We have used observed data from airglow images and lidar temperature and winds to derive the observed cancelation factor for comparison with the modeled CF. We have quantified the perturbations generated by gravity waves detected in the OH and $O(^1S)$ nightglow imagery data taken at ALO from 2015 to 2017. We provide a long-term study in calculating the magnitude of the cancelation factor, fundamental intrinsic wave parameters, and their uncertainties estimated for different solar and seasonal environment scenarios as well as different background conditions provided by the upper atmosphere climatological models (NRLMSISE-00 model) for OH and $O(^1S)$ emission. The main results of this work are:

1. Source of Discrepancies: We have found that the modeled CF relationship underestimates the observations. The disagreement shown in Figure 3 for OH emission might come from the fact that dissipative and freely propagating waves co-exist with saturated waves (as hypothesised in the CF model), and we have not separated waves by their kind in this study. That is due to the fact we do not measure individual waves simultaneously in different layers. That would be the only way to assure how the wave amplitude is affect as it moves upwards. Another possible source of inaccuracy could be introduced by the photochemical scheme used to model the cancelation factor. As we explained earlier, the model does not use realistic atomic oxygen data (see [8]) to obtain the CF magnitude. As the atomic oxygen density is affected by the season and the solar cycle activity, one way to improve the model and observation agreement is to have the O density calculated individually for each case. Beyond that, we believe that the distribution of atomic oxygen (O) with height in presence of vertically propagating waves influenced by temperature gradient that affect the rate of chemical reactions of the nightglow emissions ([5]) would be contributing to the discrepancies as well. By accounting for these discrepancies sources, it will be possible to improve the CF model for both studied airglow layers.
2. Although there are discrepancies, there are some consistency between the modeled and observed CF relationship for the $O(^1S)$ emission in the range $20 < \lambda_z < 60$ km based on the error bars and 95% confidence levels of the modeled CF, mainly for the O(^1S) layer.
3. Because the modeled CF underestimates the observed CF, we have performed a correction in the modeled CF curve by estimating the discrepancies using the observed wave data obtained from both OH and $O(^1S)$ emissions. We used for that the weighted mean and weighted standard deviation to provide a measure of the spread in the data. The have adjusted the modeled CF by the weighted mean to obtain a straightforward correction respect to the observed CF for OH and $O(^1S)$ emissions as shown in Table 5. However the observations still deviate by a factor of ~ 2 for the modeled CF$_{OH}$ showing that this simpler correction does not work for the hydroxyl emission and another strategy must be devised to improve the model and the agreement between the model and the observation.

Author Contributions: Methodology, F.V., P.V.; software, L.N., J.F, and F.V.; formal analysis, F.V., J.F.; investigation, J.F.; resources, F.V., G.S.; writing–original draft preparation, J.F.; writing–review and editing, J.F., F.V.

Acknowledgments: This research has been supported by the National Science Foundation under 1-NSF AGS Grant #17-59573 and 2-NSF AGS Grant #19-03336. We are also grateful to Mr. Luis Navarro which facilitated us the source code for airglow image processing.

Conflicts of Interest: The authors of this article declare no conflict of interest.

References

1. Hecht, J.H.; Walterscheid, R.L.; Kane, T.J.; Gardner, C.S.; Tepley, C.A. Simultaneous nightglow and Na lidar observations at Arecibo during the AIDA-89 campaign. *Journal of Atmospheric and Terrestrial Physics* **1993**, *55*, 409–423.
2. Hecht, J.H.; Walterscheid, R.L.; Ross, M.N. First measurements of the two-dimensional horizontal wave number spectrum from CCD images of the nightglow. *Journal of Geophysical Research* **1994**, *99*, 11449–11460.
3. Swenson, G.R.; Taylor, M.J.; Espy, P.J.; Gardner, C.; Tac, X. ALOHA-93 measurements of intrinsic AGW characteristics using airborne airglow imager and groundbased Na wind/temperature lidar. *Geophysical Research Letters* **1995**, *22*, 2841–2844.
4. Smith, S.M.; Mendillo, M.; Baumgardner, J.; Clark, R.R. Mesospheric gravity wave imaging at a subauroral site: First results from Millstone Hill. *Journal of Geophysical Research* **2000**, *105*, 27119–27130.
5. Swenson, G.R.; Gardner, C.S. Analytical models for the responses of the mesospheric OH* and Na layers to atmospheric gravity waves. *Journal of Geophysical Research* **1998**, *103*, 6271–6294.
6. Swenson, G.R.; Liu, A.Z. A model for calculating acoustic gravity wave energy and momentum flux in the mesosphere from OH airglow. *Geophysical Research Letters* **1998**, *25*, 477–480.
7. Liu, A.Z.; Swenson, G.R. A modeling study of O_2 and OH airglow perturbations induced by atmospheric gravity waves. *Journal of Geophysical Research (Atmospheres)* **2003**, *108*, 4151.
8. Vargas, F.; Swenson, G.; Liu, A.; Gobbi, D. O(1S), OH, and O2(b) airglow layer perturbations due to AGWs and their implied effects on the atmosphere. *Journal of Geophysical Research* **2007**, *112*.
9. Vargas, F. Uncertainties in gravity wave parameters, momentum fluxes, and flux divergences estimated from multi-layer measurements of mesospheric nightglow layers. *Advances in Space Research* **2019**, *63*, 967 – 985.
10. She, C.Y.; Yu, J.R. Simultaneous three-frequency Na lidar measurements of radial wind and temperature in the mesopause region. *Geophysical Research Letters* **1994**, *21*, 1771–1774.
11. Krueger, D.A.; She, C.Y.; Yuan, T. Retrieving mesopause temperature and line-of-sight wind from full-diurnal-cycle Na lidar observations. *Appl. Opt.* **2015**, *54*, 9469–9489.
12. Picone, J.M.; Hedin, A.E.; Drob, D.P.; Aikin, A.C. NRLMSISE-00 empirical model of the atmosphere: Statistical comparisons and scientific issues. *Journal of Geophysical Research (Space Physics)* **2002**, *107*, 1468.
13. Garcia, F.J.; Taylor, M.J.; Kelley, M.C. Two-dimensional spectral analysis of mesospheric airglow image data. *Appl. Opt.* **1997**, *36*, 7374–7385.
14. Hickey, M.P.; Yu, Y. A full-wave investigation of the use of a “cancellation factor” in gravity wave-OH airglow interaction studies. *Journal of Geophysical Research (Space Physics)* **2005**, *110*, A01301.

Table 1. The $O(^1S)$ and $OH(6,2)$ filters were used to estimate the wave amplitude based on the analytical model relating VER measured by the night airglow images to the relative atmospheric density perturbation.

Filter	λ_{center} (nm)	FWHM (nm)	Exp.time (sec)
$BG_{O(^1S)}$	551.0	3	90
$O(^1S)$	557.7	3	90
$O(^1D)$	630.0	3	75
$OH(6,2)$	840.0	20	60
$O_2(0,1)$	866.0	7	45

Table 2. This table summarizes the observing campaigns corresponding to OH and $O(^1S)$ emission lines.

Year	Month	Date	# Nights	# AGWs (OH)	# AGWs $O(^1S)$
2015	Jan-Feb	27-30, 02	5	5	5
2015	April	17-25	8	8	3
2015	July	14-25	11	11	11
2015	November	01-08	7	5	2
2016	Feb-Mar	25-29, 01-15	19	14	12
2016	June	06-11	6	6	5
2016	Oct-Nov	23-31, 01-09	17	12	4
2017	April	21-29	8	7	7
2017	November	20-28	9	7	7
2017	December	12-22	10	10	4
	10 campaigns		100	85	60

Table 3. The Lidar data summary is presented in the following table for each operation period at ALO.

Year, Month, Day	# nights	# Hours	Nights with winds (U[a],V[b])	Average CPS[c]
2015 Jan-Feb (16-31, 01-02)	16	96.4	5	559
2015 April (15-29)	14	101.9	8	556
2015 July (14-25)	11	65.3	11	554
2015 November (27-30, 01-08)	8	69.6	7	700
2016 Feb-Mar (25-29, 01-15)	19	96.7	19	540
2016 June (06-11)	6	66.0	6	760
2016 Oct-Nov (23-31, 01-04)	17	91.4	17	582
2017 April (21-29)	8	50.8	8	609
2017 November (20-28)	9	57.0	9	299
2017 December (12-24)	12	70.7	10	213
10 campaigns	155	1043.9	100	7174

[a]: U represents the zonal winds.

[b]: V represents the meridional winds.

[c]: Counts per Shot (CPS), the units of this measurement is photons/cm^2/s/W of the propagating laser power, raw photon count data are processed off-line and preliminary results are shown at the following link: http://lidar.erau.edu/data/nalidar/index.php.

Table 4. Criteria used for filtering the data-set for the OH Meinel band and $O(^1S)$ emission line.

Emission	z_r (km)	$I'/\bar{I}$	$T'/\overline{T}$	CF intensity	λ_z (km)	τ (min)
OH	88	≥ 3	$0.75 - 1.25$	≤ 10	$14 - 60$	≥ 12
$O(^1S)$	95	≥ 4	$0.75 - 1.25$	≤ 10	$10 - 60$	≥ 12

Table 5. The magnitude of the weighted mean and their errors of the direct model for the OH and $O(^1S)$ emission.

Year	CF$_{OH}$	error CF$_{OH}$	CF$_{O(^1S)}$	error CF$_{O(^1S)}$
2015	5.91	0.26	4.91	0.13
2016	5.48	0.29	4.98	0.07
2017	5.03	0.44	4.76	0.24

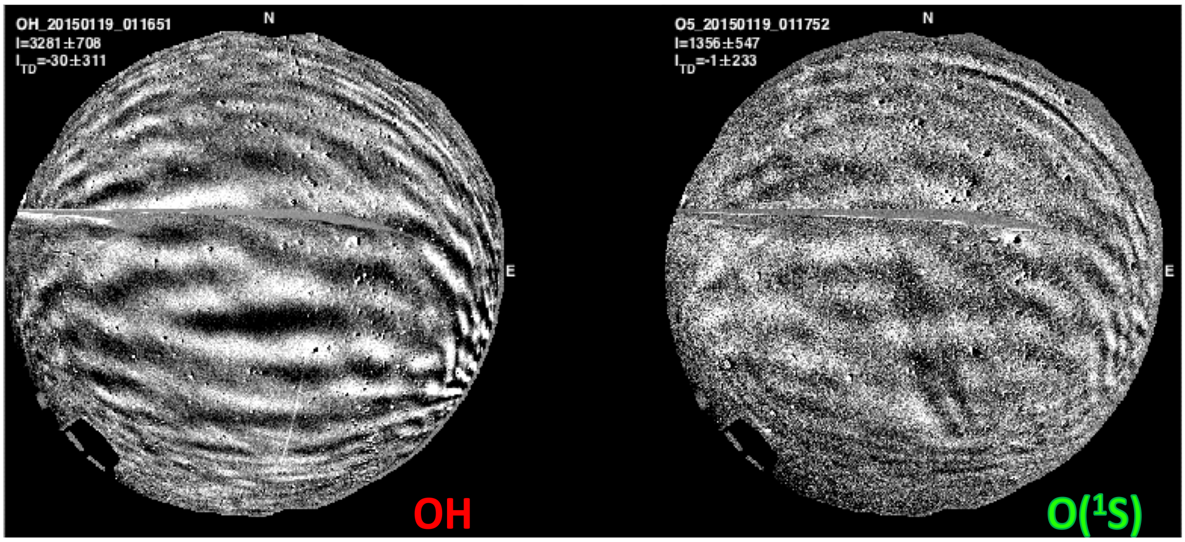

Figure 1. *OH* and $O(^1S)$ (right) night airglow emission images taken on Jan. 19, 2015 at 0116 UTC. These images are not preprocessed to show the fisheye lens distortion of the night sky. Without preprocessing, the image field of view is about 1500 km^2. Both images were captured with the ALO all-sky imaging system (ASI-1).

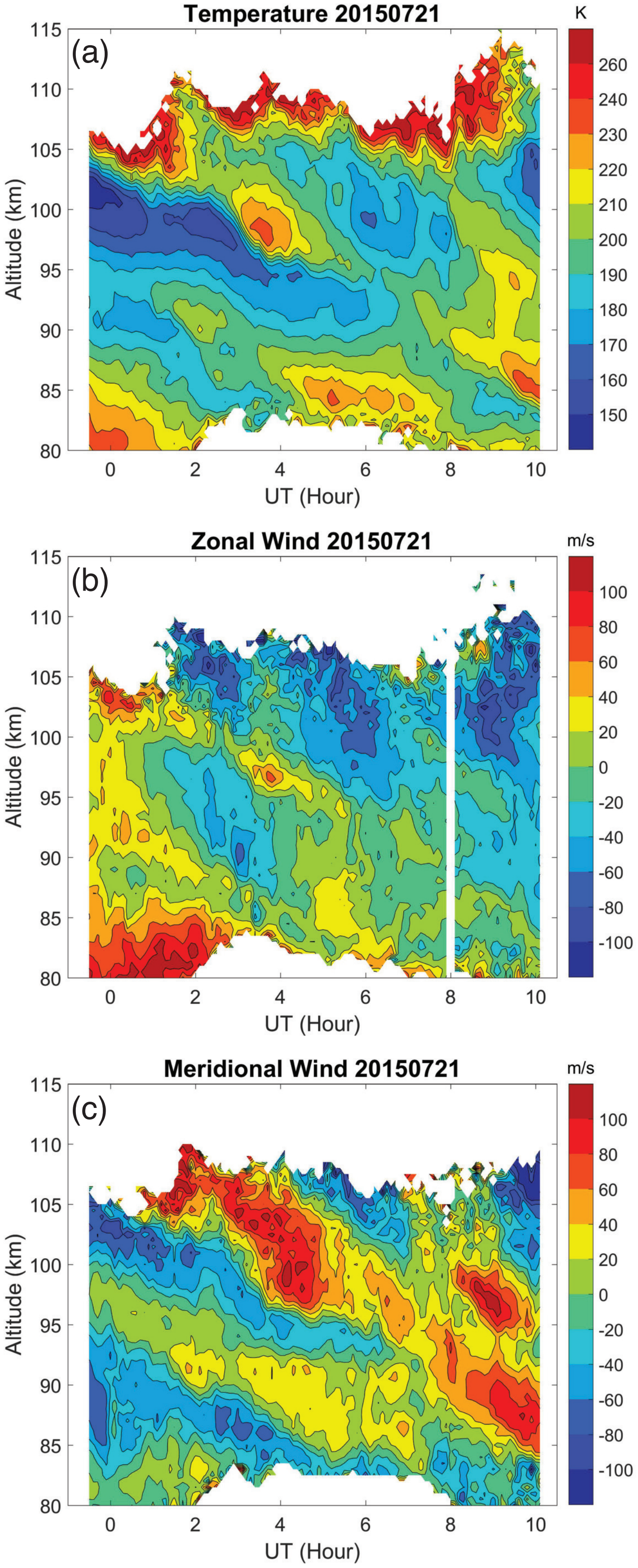

Figure 2. At the top panel is presented the meridional wind (left), vertical wind (middle), and zonal wind (right) taken on 21 July 2015. Note the nonlinear contour scale (at lowest altitudes) is used to highlight the low sensitivity of the Na winds in the mesosphere. At the bottom panel is displayed the temperature (left) and Na density (atoms per cm^3) at the right measured on the same night of 21 July 2015 by the Na lidar at Andes Lidar Observatory in Cerro Pachón, Chile.

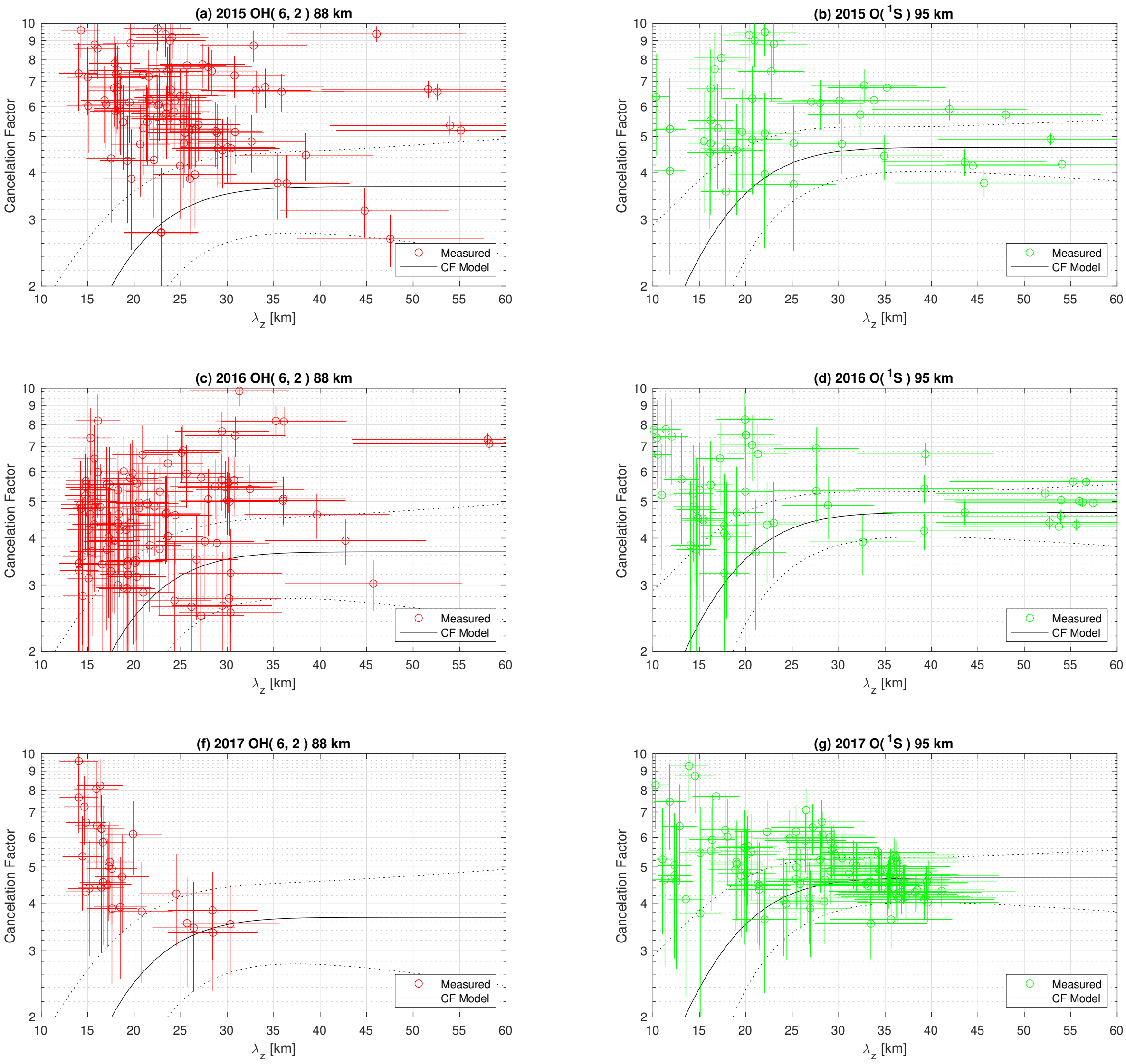

Figure 3. Cancelation factor for OH (red open circles), $O(^1S)$ (green open circles) and their errors. The dashed thin lines denote the 95% confidence bounds (2σ) around the analytic curve shown as the continuous black lines in the plots.

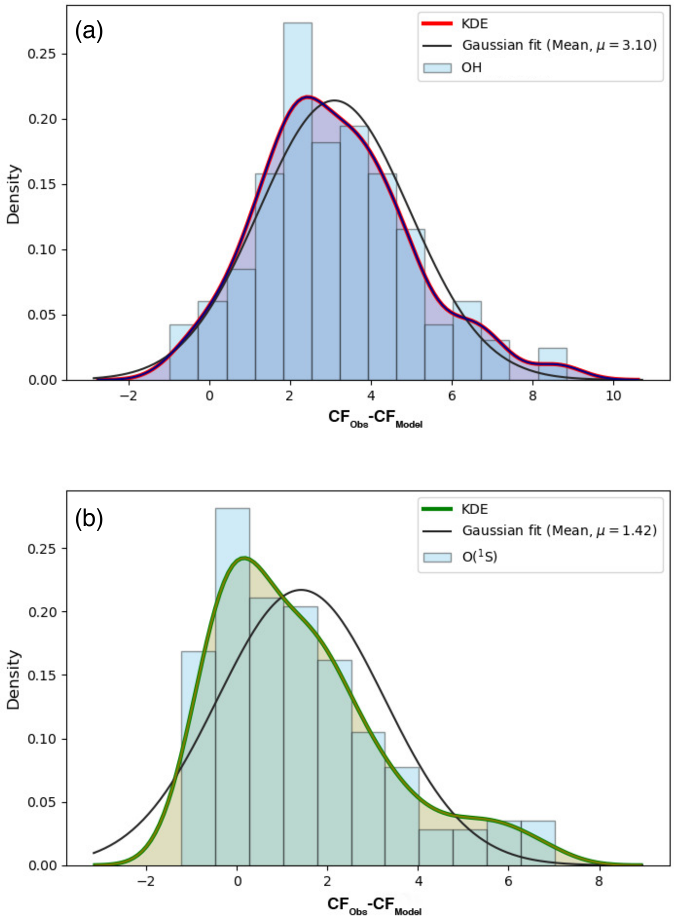

Figure 4. Histograms of the residuals and density plots for the OH and $O(^1S)$ emissions.

doi:10.20944/preprints202010.0579.v1

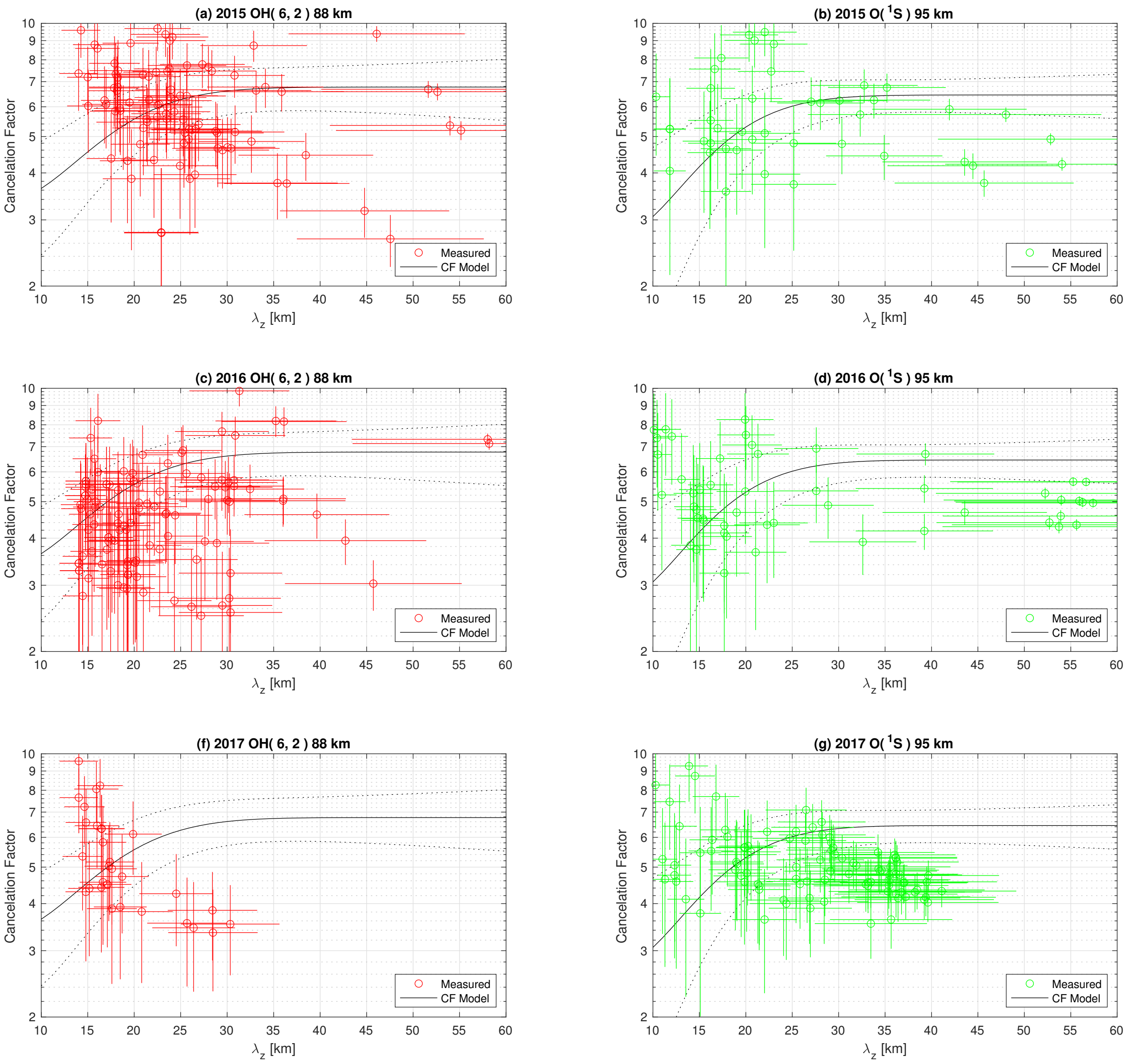

Figure 5. The plots show the observed cancelation factor corrected for both OH (red open circles) and $O(^1S)$ (green open circles) emissions and their errors. The dashed thin lines denotes the 95% confidence bounds around the analytic curve shown as the continuous black lines.